# Effects of Oxidation on Pyroxene Visible-Near Infrared and Mid-Infrared Spectra

**Molly C. McCanta[1,*], M. Darby Dyar[2]**

[1]Department of Earth and Planetary Sciences
University of Tennessee
1621 Cumberland Ave
Knoxville TN 37996
mmccanta@utk.edu

[2]Department of Astronomy
Mount Holyoke College
50 College St
South Hadley, MA 01075
mdyar@mtholyoke.edu

[*]Corresponding author

**Keywords:** cosmochemistry, geological processes, infrared observations, mineralogy

**Abstract:** Pyroxene spectral features in the visible near-infrared (VNIR) and mid-infrared (MIR) wavelengths are affected by oxidation resulting from traditional metamorphic processes as well as impact metamorphism. The observed effects are due to modifications in the crystal arising from changes in crystallization temperature or pressure or from substituting $Fe^{3+}$ for $Fe^{2+}$. Highly oxidized pyroxenes from terrestrial mantle xenoliths and shock experiments indicate that the spectral effects of oxidation are greater in clinopyroxene than orthopyroxene because clinopyroxene can accommodate more $Fe^{3+}$ structurally. Changes in clinopyroxene VNIR related to increasing oxidation include a shift in the 0.8 µm absorption band to shorter wavelengths and a strengthening of the $Fe^{2+}\leftrightarrow Fe^{3+}$ intervalence charge transfer (IVCT) band, which reduces the band depth of the 1.0 µm feature by ~20%. Although shocked clinopyroxenes are oxidized to similar levels to that seen in the mantle xenoliths, the effects of shock overprint those of oxidation in the VNIR. These include a decrease of ~76% intensity of the 2.35 µm feature and a decrease of ~70% intensity of the 1.0 µm feature. In the MIR, the effects of oxidation and shock are minimal, resulting in a 5% overall decrease in band depth. These shifts and changes can be interpreted as a result of changes in the polyhedra surrounding the Fe cations which reduce crystal field splitting and the order of the crystal structure. Determination of planetary surface composition through VNIR remote sensing methods requires careful consideration of potential changes induced via shock and/or oxidation processes.

## 1. Introduction

Pyroxene is an abundant rock-forming mineral that serves as an important recorder of petrologic processes on Earth and throughout the Solar System. Pyroxenes of various compositions have been observed in a wide-range of planetary materials including the igneous and metamorphic materials that comprise the surface and interior portions of both undifferentiated and differentiated bodies [e.g., Papike et al., 2016]. Pyroxene compositional variations can be used to determine physical conditions such as temperature, pressure, and

oxygen fugacity ($f_{O2}$) that were present in a rock's source region [e.g., Lindsley and Anderson, 1983; Mattioli and Wood, 1988; Ballhaus et al., 1990; Wood, 1991]. This combination of abundance and ability to act as a geologic recorder have made pyroxene a powerful recorder of geologic processes from the start of the Solar System through the present and made it imperative to fully identify and constrain pyroxene composition when encountered either in person or remotely.

Characterization of pyroxenes using remote sensing methods is integral to determining planetary surface compositions. Previous studies to characterize pyroxene reflectance spectra as a function of quadrilateral composition [Hamilton, 2000; Klima et al., 2007, 2011] relied on samples experimentally grown and equilibrated under reducing conditions [Turnock et al., 1973]. Spectra of natural pyroxene samples are much more complicated to interpret due to the presence of additional cations available for substitution, such as $Fe^{3+}$ and Al [i.e., Cloutis, 2002], and to geologic overprints such as oxidation or shock. It is imperative to document compositional variations outside the pyroxene quadrilateral and their effects on spectral features to better constrain planetary surface compositions.

Oxidation is a common terrestrial process, often correlated with the presence of water via metasomatic episodes. It generally results in increasing amounts of higher valence state cations, such as $Fe^{3+}$, $Cr^{3+}$, or $Ti^{4+}$. Indeed, the presence of measurable $Fe^{3+}$ in minerals and melts is often used as a proxy for $H_2O$. For example, high H diffusivities in amphibole may result in partial dehydration during ascent, removing much of the mantle water signature [Dyar et al., 1992, 1993]. The charge on the H ion is left behind in the structure during diffusion, via the dehydrogenation reaction:

$$H^{+}_{mineral} + Fe^{2+}_{mineral} \leftrightarrow \tfrac{1}{2}[H_2]_{gas} + Fe^{3+}_{mineral}.$$

Such dehydrogenation of amphibole may result in concomitant increases in $Fe^{3+}$ concentration, resulting in higher $Fe^{3+}/Fe^{2+}$ ratios. This process may also occur in pyroxenes, which have been shown to contain $H_2O$ in concentrations as high as 387 ppm in martian nakhlites (Peslier et al., 2019).

It has long been known that significant $Fe^{3+}$ substitution occurs as a result of oxidizing conditions during the crystallization of terrestrial pyroxenes [Ohashi and Hariya, 1970; Ghose et al., 1975, 1986; Akasaka, 1983; Kurepin et al., 1981]. For example, Dyar et al. [1989, 1992] and McGuire et al. [1991] studied mantle samples and noted that clinopyroxenes were typically 12-33% $Fe^{3+}$, while orthopyroxene ranged from 4-9% $Fe^{3+}$. Substitution of $Fe^{3+}$ for $Fe^{2+}$ in pyroxene cannot be charge balanced by hydrogen, but rather is accommodated by other cation substitutions in the structure, especially $Al^{3+}$ for $Si^{4+}$. The presence of such substitution presents a fundamental complication for many oxybarometers [e.g., Buddington and Lindsley, 1964; Mattioli and Wood, 1988; Ballhaus et al., 1990; Wood, 1991; Sack et al., 1980; Christie et al., 1986; Kress and Carmichael, 1991; Cottrell et al., 2009], making constraining mineral $Fe^{3+}$ contents important in the context of understanding oxygen fugacity ($f_{O2}$).

In addition to oxidation occurring via metasomatism, recent work has also documented oxidation occurring in clinopyroxene as a result of shock metamorphic processes [McCanta and Dyar, 2017]. However, it was difficult to distinguish between spectral features related to shock and those arising purely from oxidation because little data from oxidized pyroxenes were available. Here we present new VNIR and MIR data on additional shocked samples and a large range of heavily oxidized clino- and orthopyroxenes from a variety of metasomatized mantle xenoliths [McGuire et al., 1991]. The latter samples have not been subjected to shock and therefore can be used to constrain the effects of increasing oxidation state on pyroxene spectral

features. In this study we present 1) new VNIR and MIR data constraining the spectral changes observed in terrestrially oxidized pyroxenes relative to synthetic pure-$Fe^{2+}$ samples, and 2) compare the spectral features to those observed in shock oxidized pyroxenes to determine if the effects of shock and oxidation can be differentiated.

## 2. Background

Although shock likely induces both high temperatures and pressures, their collective or individual effects on pyroxene spectroscopy have not been recently studied. VNIR spectral changes with pressure, temperature, or oxidation should be seen in three types of phenomena: crystal field (CF) bands, metal-metal intervalence charge transfer (IVCT) bands, and oxygen to metal charge transfer (OMCT) transitions [Burns, 1993]. Of these, the CF bands have been well-studied under ambient conditions, most recently by Klima et al. [2008, 2010], but only decades-old data are available for other conditions. MIR spectral changes with pressure, temperature, or oxidation are less well described in the literature [e.g., Johnson et al., 2002].

In general, high temperatures are expected to cause broadening of CF bands, movement to slightly longer wavelengths, and an overall shift to lower reflectance [Burns, 1993; Hinrichs et al., 1999]. VNIR spectra of enstatite acquired at 400°C by Sung et al. [1977] show intensification of the 0.9 μm band, which indeed moves from 0.93 μm at 20°C to 0.95 μm at 400°C. However, the 1.8 μm band shift is barely resolved at 400°C due to interferences from thermal emissivity, which moves toward the visible region at those temperatures. Thus its intensity dramatically decreases with increasing temperature as thermal emission increases. Clinopyroxene (pigeonite) studied by Sung et al. [1977] shows analogous trends at VNIR wavelengths: the 0.94 μm band shifts to 0.97 between 20°C and 400°C and absorption ca. 1.8 μm decreases with increasing thermal emissivity.

Pressure effects on VNIR spectra have been studied in past decades mainly through use of static high-pressure experiments. Fe is accommodated in pyroxene in either the octahedral M1 site or the somewhat distorted 6- or 8-fold coordination M2 site (Figure 1). Pressure shifts in $Fe^{2+}$ M2 bands in orthopyroxene ranged from 12.7 up to 28.8 $cm^{-1}$/kbar [Shankland et al., 1974], i.e., a shift from 11,068 to 12,050 $cm^{-1}$ (0.90 to 0.83 μm) at 5 GPa. Ferrosilite at 2.5 GPa also shifts to higher wavenumbers (lower wavelength): 4,878 to 5411 $cm^{-1}$ (2.05 to 1.85 μm) and 10,627 to 10,693 $cm^{-1}$ (0.94 to 0.93 μm) [Mao and Bell, 1971]. Augite at 5 GPA shows blue-shift (shift to higher frequency) and increased intensity of 9,805 $cm^{-1}$ (1.02 μm) band, and almost no shift of the bands at 18,180 and 19,760 $cm^{-1}$ [Abu-Eid, 1976]. Finally, IVCT in pyroxenes was studied Bell and Mao [1974] and Mao [1970], where the 0.7 um bands was seen to intensify significantly at 30 GPa. As summarized by Burns [1993] on page 366 “in general, blue-shifts of CF absorption bands to higher energies are observed with rising pressures. With an inverse fifth-power dependence on cation-anion distance, IVCT transitions are relatively insensitive to band shifts.” Thus it is expected that the high pressures experienced during shock might have analogous effects.

Finally, it is useful to consider the effect of substituting $Fe^{3+}$ for $Fe^{2+}$ in pyroxene even at room temperature. The $Fe^{2+}$ bands arising from the M1 site occur at 10,200 $cm^{-1}$ (0.98 μm) and 8,475 $cm^{-1}$ (1.18 μm) [Rossman, 1980; Straub et al., 1991]. $Fe^{3+}$ is also thought to cause an IVCT band at 12,000-14,000 $cm^{-1}$ (0.8 to 0.7 μm) [Burns, 1993]. $Fe^{2+}$ in M2 occurs at 9,600 and 4,400 $cm^{-1}$ (1.04 and 2.27 μm) [White and Keester, 1966; Burns and Huggins, 1973; Hazen et al., 1978]. $Fe^{3+}$ is thought to occupy only the M1 site, so its substitution should thus affect only the ~1 μm region unless the $Fe^{3+}$ substitution affects the overall geometry of the mineral. In such

cases spin-forbidden crystal field transitions in $Fe^{3+}$-bearing clinopyroxene can result in a sharp peak near 0.44 μm as well as two broad bands near 0.82 and 0.60 μm [Burns et al., 1976; Rossman, 1980]. These features are often too weak to be detected in reflectance spectra, masked by the $Fe^{2+} \leftrightarrow Fe^{3+}$ IVCT band.

All of these spectral band shifts result from changes in the geometry and size of the oxygen polyhedra surrounding the $Fe^{2+}$ and $Fe^{3+}$ cations in the pyroxene structure. Insights into these shifts can be gained by comparisons of the crystal structures of hedenbergite synthesized at 0 and 10 GPa ($CaFe^{2+}Si_2O_6$ from Zhang et al. [1997]) compared with the $Fe^{3+}$ pyroxene end-member esseneite ($CaFe^{3+}AlSiO_6$, from Cosca and Peacor [1987]). Portions of these three structures are shown in Figure 1 from the same perspective, looking down the *x* axis.

Close inspection of Figure 1 reveals subtle differences between these three spectra that are quantified in Figure 2, which shows the cation-oxygen bond distances. Compared with 0 GPa hedenbergite, both the shocked and oxidized pyroxenes show longer FeM2-O1, FeM2-O2, and M2-O3 bond distances. Shocked hedenbergite also has the longest M2-O3 bonds and M1-O1 and M1-O2 as well. Longer bond distances imply higher values of crystal field splitting [Burns, 1993], which is expressed in wavenumbers, and thus high pressure/shock would be expected to shift peaks to lower wavelengths in VNIR spectra.

In summary, prior research on the effects of temperature, pressure, and changes in polyhedral size due to oxidation (substitution of smaller trivalent cations such as $Fe^{3+}$) are all known to affect the positions and intensities of pyroxene spectral bands. This paper seeks to clarify which of these effects is dominant relative to oxidation state and shock phenomena.

## 3. Samples studied

### *3.1. Terrestrial mantle pyroxenes*

Spinel lherzolite xenoliths from Dish Hill and Cima, CA, and Kilbourne Hole, NM were gently crushed and hand-sieved to avoid potential oxidation. Orthopyroxene and clinopyroxene were hand-picked to create mineral separates that were visually pure and their $Fe^{3+}/\Sigma Fe$ was determined via Mössbauer spectroscopy (Table 1; Figure 3) following methods of Dyar et al. [1989] and McGuire et al. [1991]. In previous work, highly oxidized pyroxenes like these were interpreted to be the result of metasomatic processes active in the upper mantle [McGuire et al., 1991]. All pyroxenes are Mg-rich because they represent high temperature crystallization products of mantle assemblages, with the majority of compositions falling between the enstatite and diopside end-members (Figure 3).

### *3.2. Shocked pyroxenes*

The target sample used in the shock experiments was a diopside from Jaipur, India ($Wo_{49}En_{47}Fs_4$) with low starting $Fe^{3+}$ (9%) (Table 1; Figure 3). All shock experiments were performed at Johnson Space Center utilizing a 20 mm flat plate accelerator [Hörz, 1970]. Samples were prepared asparticulate material sieved to a grain size of 150-250 μm [McCanta and Dyar, 2017]. The prepared targets were encased in stainless steel containers. Projectiles were composed of polyethylene mounted with metal flyer plates of varying composition determined by the desired shock pressure. Experiments were run over a range of shock pressures from 21 to 59 GPa (Table 1) and took place under vacuum, at relatively high $p_{O2}$ conditions (~$10^{-4}$ atm). All pyroxenes were analyzed with Mössbauer spectroscopy post-experiment and observed to be oxidized relative to the starting diopside regardless of shock pressure [McCanta and Dyar, 2017].

## 4. Analytical Methods

### *4.1. Reflectance spectroscopy*

Shocked and natural samples were gently ground to make a whole-rock powder, which was sieved to <45 μm prior to spectral analysis. Visible to near-infrared bi-directional reflectance spectra (0.3-2.6 μm, sampled at 5 nm increments) were acquired relative to halon at 30° incident, 0° emergent angles using the Reflectance Experiment Laboratory (RELAB) bidirectional spectrometer at Brown University. Data were then corrected for the properties of halon.

The same samples (in the same dish) were measured using a Pike diffuse reflectance attachment (off-axis, biconical) with the Thermo Nexus 870 FTIR spectrometer (2-50 μm, 5000-200 $cm^{-1}$) located at RELAB, using a diffuse gold standard. FTIR spectra were obtained in a purged environment ($H_2O$ and $CO_2$ free). Data were typically spliced to the near-infrared data at 2.5 μm to use the absolute reflectance of the bidirectional system. Detailed descriptions of the RELAB facility instruments can be found in the overview by Pieters and Hiroi [2004] (RELAB information is also available at http://www.planetary.brown.edu/relab/).

All band depths were calculated using methods developed in Pelkey et al. [2007] where absorption band depths (BD) are determined according to Eq. 1.

$$BD = 1 - R_C/R_{C*}, \quad (1)$$

where $R_C$ is the reflectance at the center of the spectral band and $R_{C*}$ is the modeled reflectance at the center of the band (defined in Eqs. 2-4).

$$R_{C*} = aR_S + bR_L \quad (2)$$

$$a = b-1 \quad (3)$$

$$b = (\lambda_C-\lambda_S)/(\lambda_L-\lambda_S) \quad (4)$$

$R_{C*}$ is therefore a linear fit between the long wavelength ($\lambda_L$) and short wavelength ($\lambda_S$) areas outside the designated band.

### *4.2. Mössbauer spectroscopy*

Approximately 40 mg of each sample were gently mixed with sugar under acetone (to prevent oxidation via heating), then heaped in a sample holder confined by Kapton ® polyimide tape. Mössbauer spectra were acquired at 295K using a source of ~80 mCi $^{57}Co$ in Rh on a SEE Co. (formerly WEB Research Co.) model WT302 spectrometer (Mount Holyoke College). For each sample, the fraction of the baseline due to the Compton scattering of 122 keV gammas by electrons inside the detector was determined by measuring the count rate with and without a 14.4-keV stop filter (~2 mm of Al foil) in the gamma beam. Compton-corrected absorption was calculated for each individual spectrum using the formulation A/(1 - b), where b is the Compton fraction and A is the uncorrected absorption. This correction does not change the results of the fits per se but does allow accurate determination of % absorption in the spectra. It is necessary because the range of energy deposited in the detector by Compton events extends from 0 keV to 40 keV, overlapping both the 14 keV and 2 keV energies deposited by the 14 keV gammas.

Run times were 24-48 hours. Spectra were collected in 2048 channels and corrected for nonlinearity via interpolation to a linear velocity scale, which is defined by the spectrum of the 25 μm Fe foil used for calibration. The WMOSS algorithm fits a straight line to the points defined by the published values of the Fe metal peak positions (as *y* values) and the observed positions in channels (*x* values). Data were then folded before fitting, using the WMOSS Auto-fold procedure that folds the spectrum about the channel value that produces the minimum least

squares sum difference between the first half of the spectrum and the reflected second half of the spectrum.

Mössbauer spectra were modeled using the Mex_disdd program, which was acquired from the University of Ghent courtesy of E. DeGrave. The program uses Lorentzian line shapes and solves full hyperfine interaction Hamiltonians for isomer shift and quadrupole splitting but uses multiple distributions for magnetically split spectral components, where the value of the magnetic field is given as the value for the most heavily weighted distribution. Errors on isomer shift, quadrupole splitting, and line widths are ±0.02-0.03 mm/s for the doublets and sextets in these spectra, and errors on hyperfine fields are ±2-3 kOe. Errors on total $\%Fe^{3+}$ are ±1-5 % absolute based on repeated fits to the same spectra, with a detection limit for $Fe^{3+}$ of roughly 1%. Spectra from McCanta and Dyar (2017) were re-fit for this project to ensure consistency; resultant changes were within error bars for the technique as quoted above.

## 5. Results

### *5.1. Mössbauer results*

Much has been written to explain site assignments used to interpret Mössbauer spectra of pyroxenes; see Dyar et al. [2013] for a summary. In brief, there are up to three $Fe^{2+}$ doublets arising from $Fe^{2+}$ in some combination of M1 and M2 sites, but assignment of those doublets has varied. In orthopyroxene, Seifert [1983] suggested that minor substitution of trivalent cations ($Fe^{3+}$ and $Al^{3+}$) into M1 causes distortion in adjacent M2 site. Seifert [1983] posited two types of M1 sites: one with only divalent neighbors, and one with trivalent substitutions in adjacent sites.

In clinopyroxene, Dowty and Lindsley [1973] interpreted their spectra to represent one $Fe^{3+}$, one $^{M2}Fe^{2+}$ and two $^{M1}Fe^{2+}$ doublets; Zhi et al. [2001] concurred with these assignments and suggested that $Fe^{3+}$ was in M1. Many subsequent papers [e.g., Dyar et al. 1989 and Dyar et al. 2013] also observed the three $Fe^{2+}$ doublets in pyroxenes, but reversed the site assignments to two $^{M2}Fe^{2+}$ and one $^{M1}Fe^{2+}$ doublets. In the latter study of synthetic Ca-Mg-Fe clinopyroxenes, all samples with $Ca^{2+}$ > Mg+Fe displayed the one M1 and two M2 $Fe^{2+}$ doublets, each with a distinctive recoil-free fraction. The second M2` site was suggested by Rossi et al. [1987] and Bruno et al. [1982] to be the location for divalent cations, leaving the M2 for Ca. However, Mössbauer data are most consistent with the presence of some $Fe^{2+}$ coexisting with Ca in M2, some in M2`, as well as with other cations in M1. Thus, three $Fe^{2+}$ doublets are seen in some of our pyroxene data and assigned as M1, M2, and M2`. Note that one sample (Ba-2-101-B opx) also contained an olivine impurity, distinctive due to its high quadrupole splitting and constrained by the four-phase mineral assemblage in these rocks.

Those site assignments are given in Table 2 in the Appendix following conventions established in Dyar et al. [2013] for $Fe^{2+}$. The site with isomer shift (δ) of ~1.18 mm/s and quadrupole splitting (Δ) of ~2.50 mm/s is assigned to $Fe^{2+}$ in M1, $\delta \approx 1.14$ mm/s and $\Delta \approx 2.0$ mm/s to $Fe^{2+}$ in M2, and $\delta \approx 1.14$ mm/s, and $\Delta \approx 1.80$ mm/s to $Fe^{2+}$ in M2`. Site assignments for $Fe^{3+}$ features have not been well-established, although it is generally assumed that the smaller $Fe^{3+}$ cations will occupy solely the M1 site or possibly substitute for $Si^{4+}$ in the tetrahedral site. We have labeled the $Fe^{3+}$ doublets as $^{A}Fe^{3+}$, $^{B}Fe^{3+}$, and $^{iv}Fe^{3+}$ for now, pending eventual completion of single crystal structure refinements (SREF) that are in progress.

$Fe^{3+}$ is determined directly from peak areas with no correction to account for differential for recoil-free fraction, *f*, for $Fe^{2+}$ and $Fe^{3+}$. At 295K, values of *f* have been well-characterized for $Fe^{2+}$ in M1 and M2 in pyroxene [Dyar et al., 2007, 2013] and are quite similar. However, to our

knowledge, *f* has not been measured for $Fe^{3+}$ in pyroxene, and therefore no correction could be made. Note also that spectra with the identical proportion of Fe in any given site may not have the same site occupancies because Mössbauer only measures *percentages* of the total Fe cations present rather than the *total* Fe cations. Thus this study focuses on $Fe^{3+}$ contents rather than on site occupancies of Fe, which are the subject of ongoing work in our group. The percentage of the total Fe as $Fe^{3+}$ in our suite ranges from 4 to 14% in orthopyroxene and 8 to 54% in clinopyroxene. These ranges are consistent with those observed for these minerals by Dyar et al. [1989], McGuire et al. [1991], and Dyar et al. [1992].

*5.2. VNIR results*

$Fe^{3+}/\Sigma Fe$ contents in the mantle clinopyroxene range from 0.09-0.40 (Table 1), indicating significant $Fe^{3+}$ can substitute into the mineral structure. The metasomatized mantle clinopyroxene VNIR features show typical clinopyroxene spectral features including 1.0 µm and 2.35 µm features resulting from $Fe^{2+}$ in the M2 site and a $Fe^{2+} \leftrightarrow Fe^{3+}$ intervalence charge transfer (IVCT) band near 0.8 µm (Figure 4). Both the 1.0 µm and the 0.8 µm bands broaden as the amount of $Fe^{3+}$ increases in the clinopyroxene, with the 0.8 µm feature shifting to lower wavelengths (~0.75 µm; Figure 4). The strengthening of the $Fe^{2+} \leftrightarrow Fe^{3+}$ IVCT band also results in the reduction of the band depth of the 1.0 µm feature (~20%) with progressive oxidation. Although the Mössbauer data show the presence of some $Fe^{2+}$ in the M1 site that should give rise to bands ca. 1.0 and 1.2 µm, those are not apparent in the VNIR spectra. Perhaps they overlap with the 1.0 µm feature from $^{M2}Fe^{2+}$ and/or are not seen because the total $^{M1}Fe^{2+}$ is very small, about 0.05 formula units or less. A number of the mantle clinopyroxenes exhibit a strong 0.64 µm band related to Cr content [Cloutis, 2002] (Figure 4). Additionally, the presence of spin-forbidden $Fe^{3+}$ is observed as a weak, sharp peak near 0.44 µm in the oxidized samples (Figure 4). Spin-forbidden $Fe^{3+}$ features at 0.6 and 0.82 µm are not observed as they are obscured by the Cr content of the pyroxene or the $Fe^{2+} \leftrightarrow Fe^{3+}$ IVCT band, respectively.

The mantle orthopyroxene samples analyzed contain significantly less $Fe^{3+}$ than the associated clinopyroxenes ($Fe^{3+}/\Sigma Fe$ = 0.06-0.14) due to steric constraints [e.g., McGuire et al., 1991]. The grains exhibited typical VNIR features including band minima at 0.9 and 1.8 µm resulting from $Fe^{2+}$ in the M2 site (Figure 5). The more oxidized samples show a slight increased absorption around 0.65 µm due to the presence of a $Fe^{2+} \leftrightarrow Fe^{3+}$ IVCT band. No indication of hematite is present in the analyzed orthopyroxene samples [i.e., Straub and Burns, 1991], though the low overall $Fe^{3+}$ content of the orthopyroxenes may prevent this.

The experimentally shocked clinopyroxene showed significant $Fe^{3+}$ concentrations (unshocked: 9% → shocked average: 25% $Fe^{3+}$) accompanied by an overall flattening of VNIR spectral features (Figure 6). With shock metamorphism, there is a decrease of ~76% intensity of the spectral band arising from $Fe^{2+}$ in the M2 site at 2.35 µm. In addition, a decrease of ~70% intensity of the spectral band arising from $Fe^{2+}$ in the M2 site at 1.0 µm was observed (Figure 6). A commensurate increase in band intensity for $Fe^{3+}$ features, such as the $Fe^{2+} \leftrightarrow Fe^{3+}$ IVCT band, was not observed likely because they are of such low intensity and therefore overshadowed by the shock-induced destruction of VNIR features. No correlation of total shock pressure and amount of $Fe^{3+}$ present in the clinopyroxene is observed.

Oxidation is also recorded in the VNIR region as a strong inverse relationship between spectral slope from 0.4 and 0.6 µm (absorption edge) and $\%Fe^{3+}$ in the shocked pyroxenes with a 67% decrease in slope recorded as oxidation increases (Figure 7), although there is not a direct correlation between increasing amount of shock pressure and slope decrease (i.e., the least

shocked sample at 36 GPa exhibits the largest decrease in spectral slope). A similar inverse relationship occurs in the oxidized mantle clinopyroxenes (73% decrease in slope of the absorption edge as oxidation increases) albeit offset to higher slope values (Figure 7). Orthopyroxenes, which have low $Fe^{3+}/\Sigma Fe$ due to steric crystal chemical constraints, do not appear to have a similar correlation.

*5.3. MIR results*

The shocked clinopyroxenes and the unshocked starting material all exhibit the five critical absorptions in the MIR denoted by Hamilton [2000] in reduced synthetic samples (CA1 = 1120 $cm^{-1}$; CA2 = 961 $cm^{-1}$; CA3 = 916 $cm^{-1}$; CA4 = 560 $cm^{-1}$; CA5 =482 $cm^{-1}$). However, the band centers have been offset to slightly different wavelengths due to different compositions (CA1 = 1138 $cm^{-1}$; CA2 = 963 $cm^{-1}$; CA3 = 923 $cm^{-1}$; CA4 = 565 $cm^{-1}$; CA5 = 474 $cm^{-1}$) (Figure 8). In addition, the 515 $cm^{-1}$ spectral absorption generally observed in high Mg pyroxenes is also present in both shocked and unshocked clinopyroxenes. The shocked clinopyroxenes however are demonstrably different from the unshocked starting material. Most notably, there is a decrease in overall band depth of ~5% at all shock pressures (Figure 8), similar to that described in shocked orthopyroxenites [Johnson et al., 2002]. Additionally, there is a significant shift in the transparency feature whose center is located at 742 $cm^{-1}$ in the unshocked material and shifted to higher wavenumbers (798 $cm^{-1}$) in all shocked clinopyroxenes (Figure 8). No obvious correlation with amount of band depth decrease and shock pressure is observed.

The oxidized mantle clinopyroxenes exhibit the CA1, CA4, and CA5 critical MIR absorptions in addition to the 515 $cm^{-1}$ absorption [Hamilton, 2000] (Figure 9). The two absorption features at 923 and 963 $cm^{-1}$ are muted, instead a single broad feature centered at 943 $cm^{-1}$ is observed (Figure 9). A decrease in the overall band depth of ~5%, similar to that seen in the shocked clinopyroxenes is evident when comparing the low $Fe^{3+}$ clinopyroxenes to those with high $Fe^{3+}$ (Figure 9) with the 943 $cm^{-1}$ absorption showing the most significant decrease (~22%).

All critical absorption features identified by Hamilton [2000] in high Mg orthopyroxene MIR spectra were observed in the mantle orthopyroxenes in this study (CA1 = 1090 $cm^{-1}$; CA2 = 980 $cm^{-1}$; CA3 = 957 $cm^{-1}$; CA4 = 868 $cm^{-1}$; CA5 = 570 $cm^{-1}$; CA6 = 548 $cm^{-1}$; CA7 = 511 $cm^{-1}$; CA8 = 451 $cm^{-1}$) (Figure 10). The broad nature of the CA1 feature makes it difficult to assign an absolute position, but it remains close to that determined for high Mg orthopyroxene. The amount of $Fe^{3+}$ substitution into the mantle orthopyroxenes studied is small when compared to that of the clinopyroxenes. As such, no differences are observed as a function of increasing $Fe^{3+}$ concentration (Figure 10).

## 6. Discussion

*6.1. Effects of oxidation on pyroxene spectra*

The effects of oxidation on pyroxene VNIR spectra can be summarized as a shift in the 0.8 µm feature to lower wavelengths and a strengthening of the $Fe^{2+} \leftrightarrow Fe^{3+}$ intervalence charge transfer (IVCT) band, reducing the band depth of the 1.0 µm feature. Recall that the introduction of $Fe^{3+}$ in the pyroxene structure increases the FeM2-O1, FeM2-O2, and M2-O3 bond distances. The higher crystal field splitting would imply a shift to lower wavelength of the M2 bands, and that is indeed what is observed. It is also logical to conclude that the increase in IVCT band strength results from the higher $Fe^{3+}$ contribution to it. Additionally, oxidation results in an

366 inverse relationship between the spectral slope in the absorption edge and the %$Fe^{3+}$. Shock can
367 be ruled out as contributing to this feature as similar changes are observed in oxidized samples
368 from both shock experiments and natural mantle assemblages (Figure 7).
369
370 *6.2. Effects of shock on pyroxene spectra*
371 Shock overprints these effects in the VNIR and results in a decrease of ~76% intensity of
372 the 2.35 μm feature and a decrease of ~70% intensity of the 1.0 μm feature. Although all
373 pyroxenes analyzed in this study were oxidized, clear differences exist between their spectra.
374 The effect is most striking in the VNIR region. When comparing shocked and unshocked
375 clinopyroxenes with similar $Fe^{3+}$ contents (31% vs. 35%), the spectral band at 2.35 μm,
376 representative of $Fe^{2+}$ in the M2 site, is nearly completely gone in the shocked sample while it
377 remains unchanged in the oxidized sample (Figure 11). The depth of the 1.0 μm band that
378 reduces as oxidation progresses in the mantle clinopyroxene is similarly reduced in the shocked
379 samples, but to a much larger degree (80% reduction in intensity when $Fe^{3+}$ is controlled for;
380 Figure 11). The slight shift in the position of the 1.0 μm band between the plotted pyroxenes may
381 be due to the compositional difference between the mantle clinopyroxene and shocked starting
382 material and/or it could be a shock effect. Finally, the 0.8 μm $Fe^{2+}\leftrightarrow Fe^{3+}$ IVCT band is not
383 present at all in the shock oxidized clinopyroxenes although visible in the mantle oxidized
384 samples. For the studied clinopyroxenes, the effects of shock appear to overprint those of
385 oxidation in the VNIR region.
386 Based on the background presented earlier, it would be expected that the effects of high
387 temperature experienced during shock, if quenched in the structure, would result in broadening
388 and redshift of crystal field bands. This is not seen. Pressure effects from shock should be
389 manifest as blueshifts to lower wavelengths of both $^{M2}Fe^{2+}$ bands potentially accompanied by
390 intensification of IVCT features. Only the first of these is observed, accompanied by the
391 disappearance of the 2.35 μm band and a very diminished 1.0 μm band. These results suggest
392 that shock is reducing the size of the polyhedra surrounding the Fe cations, reducing CF splitting
393 and order of the crystal structure and blueshifting the peaks. However, at some point in the shock
394 process, the long-range order in the structure breaks down completely. Some CF splitting
395 remains at 1.0 μm but not at 2.35 μm. It is possible that the M2 site falls apart because it is larger
396 and thus more vulnerable to distortion and disintegration from shock. This might leave only a
397 small 1.0 μm feature from M1. Moreover, IVCT is no longer possible because the regular atomic
398 structure that permits exchange of electrons between Fe cations in adjacent sites no longer exists.
399 Confirmation of the nature of the residual structure of shocked pyroxenes remains elusive to our
400 efforts to date; so far, we have not succeeded in finding well-diffracting crystals from any
401 meteorite to examine the extent of ordering (though we are continuing to try).
402 In the MIR, both shocked oxidized and mantle oxidized clinopyroxenes show a decrease
403 in band depths of absorption features of similar magnitude. The most obvious difference between
404 the samples is the CA2 and CA3 features which are both observed in the shocked clinopyroxenes
405 (Figure 8) but are combined into a single broad feature in the mantle clinopyroxenes (Figure 9).
406
407 *6.3. Crystallographic controls on $Fe^{3+}$ incorporation in pyroxene*
408 Steric controls prevent significant incorporation of $Fe^{3+}$ into the orthopyroxene crystal
409 structure though some substitution does occur ca. 0-16% of $Fe^{3+}/\Sigma Fe$ [e.g., Annersten et al.,
410 1978; Canil et al., 1994; McGuire et al. 1989, 1991; Dyar et al. 1989, 1992]. However, this study
411 and many prior ones have demonstrated that clinopyroxene can accommodate significant

($Fe^{3+}/\Sigma Fe$ values of 10-66%) amounts of $Fe^{3+}$ into its structure [McGuire et al. 1989, 1991; Dyar et al. 1989, 1992]. The presence of $Fe^{3+}$ in clinopyroxene is controlled not only by redox state (i.e., the amount of $Fe^{3+}$ present in the system to be incorporated into the crystal), but also by the pyroxene Mg# (= $Mg/Mg+Fe^{2+}$). Clinopyroxenes with Mg# >90 exhibit $Fe^{3+}/\Sigma Fe$ concentrations of less than 20% (Table 1). Those pyroxenes with Mg# 80-90 contain significantly more $Fe^{3+}$ (Table 1). It may be this correlation results from the overall bulk concentration of iron in the system such that when more iron present more is available to be oxidized. This is complicated by temperature and pressure controls as well, although these should be minimized in this sample set as all pyroxenes come from similar mantle xenoliths. This question will be resolved in our ongoing program to obtain SREF on all these samples where possible.

*6.4. Comparison with previous studies*

Previous studies have looked at the effects of either shock [Jeanloz and Ahrens, 1977; Adams et al., 1979; Johnson et al., 2002] or oxidation [Cloutis, 2002] in pyroxene spectra separately. In contrast to the significant changes in the shocked pyroxene VNIR spectra discussed in this study, Adams et al. [1979] observed no change in pyroxene VNIR spectra at experimental shock pressures of 59.7 GPa. An experimental study of the effects of increasing shock pressure on MIR spectra of orthopyroxenites (bronzite-rich) found little change beyond a general shallowing of minor absorption features at 976 $cm^{-1}$ and 567 $cm^{-1}$ [Johnson et al., 2002]. Direct comparisons cannot be made with the shocked pyroxenes in this study and those in previous studies due to starting composition differences (clinopyroxene vs. orthopyroxene). The crystallographic and crystal chemical changes associated with these differences are significant. Clinopyroxene appears to behave in a different manner when subjected to high shock pressures (30-59 GPa) resulting in changes to characteristic VNIR spectral features, including loss of the 2.35 µm band and shallowing of the 1.0 µm band, and decreasing band depths in the MIR (Figures 4 and 8).

Shock oxidation has also been observed in the mafic mineral olivine in experimental samples where the shock took place under high $p_{O2}$ conditions [Bauer, 1979]. Shock oxidation in natural olivine has proven more difficult to quantify. Ostertag et al. [1984] proposed shock oxidation as the reason for the brown olivine observed in martian meteorite ALHA 77005, although Burns [1989] showed that minimal $Fe^{3+}$ (<1%) was present in the natural shocked olivines. A more recent study of martian chassignite NWA 2737 reported shocked olivine with up to 3% total iron as $Fe^{3+}$ [Treiman et al., 2007; Pieters et al., 2008] suggesting the potential for some production of $Fe^{3+}$ during the shock process. The amounts of $Fe^{3+}$ proposed for olivine incorporation are very small due to crystallographic controls

*6.5. Implications for remote sensing*

Assigning values to the location of the 1.0 µm (Band 1) and 2.0 µm (Band 2) pyroxene VNIR features remains one of the most common means by which to determine planetary surface compositions remotely [e.g., Adams, 1974; Pieters, 1993; Mustard et al., 2005; Burbine et al., 2010]. Even the high levels of $Fe^{3+}$ incorporation measured in the oxidized mantle clinopyroxene samples do not significantly change the location of either of these features in either the studied ortho- or clinopyroxene. However, either the shifting of the $Fe^{2+} \leftrightarrow Fe^{3+}$ IVCT band from near 0.8 µm to ~0.75 µm as a function of progressive oxidation in the clinopyroxene or the observation of the weak, but sharp peak at 0.44 µm due to spin-forbidden $Fe^{3+}$ (Figure 4) could be used to determine if the clinopyroxene was oxidized (i.e., contained significant amounts of $Fe^{3+}$). This

shift was not observed in the orthopyroxene samples, although the low total $Fe^{3+}$ contents of those grains might hinder this.

It may also be feasible to use the negative slope observed in the absorption edge as a function of $\%Fe^{3+}$ to quantify clinopyroxene oxidation state remotely (Figure 7). The oxidized mantle samples exhibit this correlation. Significantly, the shock oxidized samples do as well. Although shock appears to obliterate much of the oxidized spectral signal (Figure 11), the negative slope of the absorption edge remains. Therefore, the shifting of the $Fe^{2+}\leftrightarrow Fe^{3+}$ IVCT band could be used to determine that a clinopyroxene was oxidized and the slope of the absorption edge could determine the degree of that oxidation.

A more significant implication for remote sensing studies of planetary surfaces is the effect of shock. The 2.35 µm feature suffers a decrease of ~76% in spectral intensity via shock processes (Figure 6), although a minor band is still present at all shock pressures studied. In the absence of this feature, pyroxene presence and composition cannot be determined using VNIR observations alone. The 1.0 µm feature remains in our shock experiments, although the band depth is greatly diminished, suggesting that higher shock pressures might result in its loss as well. MIR pyroxene spectral features are minimally affected by shock (Figure 8) and therefore could be used to identify the presence of pyroxene even if shocked. Therefore, a combination of wavelengths may be required to accurately identify and determine pyroxene composition remotely. Careful consideration of both VNIR and MIR wavelengths collectively may also allow for information about the shock and/or oxidation history of the pyroxene to be evaluated which would not be possible individually.

## 7. Conclusions

The effects of shock on pyroxene spectra are most prevalent in the VNIR, causing an overall flattening of spectral features. Decreases in band depth due to shock are also observed in the MIR, but to a much smaller degree. The effect of oxidation on pyroxene spectra is observed in VNIR spectra of clinopyroxenes as an overall shallowing of slope from 400 to 600 nm and a shifting of the $Fe^{2+}\leftrightarrow Fe^{3+}$ IVCT band with progressive oxidation. This is observed in all oxidized samples, both shock-oxidized and mantle, and results from the charge transfer reactions at these wavelengths. Oxidation effects in the MIR were minimal and do not appear to be linked to pyroxene $\%Fe^{3+}$ concentration. It is evident that when interpreting spectral data from surfaces that may contain pyroxene, especially clinopyroxene, the effects of shock and oxidation need to be considered.

**Acknowledgments.** Work supported by NSF grants EAR-1754268 and EAR-1754261 and NASA grant 80NSSC19K1008. We thank Takahiro Hiroi for assistance collecting VNIR and MIR data at RELAB and Elizabeth Sklute for assistance with Mössbauer data processing. The reviews of Jeff Johnson and an anonymous reviewer were thorough and much appreciated.

497 **References**


498 Abu-Eid, R. M. (1976) Absorption spectra of transition metal-bearing minerals at high pressures.
499 In *The Physics and Chemistry of Rocks and Minerals*. R.G.J. Strens, ed., Wiley, New
500 York, pp. 641-675.
501 Adams, J.B. (1974) Visible and near-infrared diffuse reflectance spectra of pyroxenes as applied
502 to remote sensing of solid objects in the solar system. Journal of Geophysical Research
503 79, 4829-4836.
504 Adams, J.B., Hörz F., and Gibbons R.V. (1979) Effects of shock-loading on the reflectance
505 spectra of plagioclase, pyroxene, and glass. 10th Lunar and Planetary Science Conference,
506 1-3.
507 Akasaka, M. (1983) $^{57}$Fe Mössbauer study of clinopyroxenes in the join $CaFeAlSiO_6$-$CaTiAlO_6$.
508 Physics and Chemistry of Minerals, 9, 205-211.
509 Annersten H., Olesch M., and Seifert F.A. (1978) Ferric iron in orthopyroxene: a Mössbauer
510 spectroscopic study. Lithos 11, 301-310.
511 Ballhaus C., Berry R.F., and Green D.H. (1990) Oxygen fugacity in the Earth's upper mantle.
512 Nature 348, 437-440.
513 Bauer J.F. (1979) Experimental shock metamorphism of mono- and polycrystalline olivine: A
514 comparative study. 10th Lunar and Planetary Science Conference, 2573-2596.
515 Bell P.M. and Mao H.K. (1974) Pressure effect on charge-transfer processes in minerals.
516 Carnegie Institution of Washington Yearbook 73.
517 Buddington A.F. and Lindsley D.H. (1964) Iron-titanium oxide minerals and synthetic
518 equivalents. Journal of Petrology 5, 310–357.
519 Bruno, E., Carbonin, S., and Molin, G. (1982) Crystal structures of Ca-rich clinopyroxenes on
520 the $CaMgSi_2O_6$-$Mg_2Si_2O_6$ join. Tschermaks Mineralogische und Petrographische
521 Mitteilungen, 29, 223-240.
522 Burbine T.H., Buchanan P.C., Dolkar T., and Binzel R.P. (2010) Pyroxene mineralogies of near-
523 Earth vestoids. Meteoritics and Planetary Science 44, 1331-131.
524 Burns R.G. (1989), Olivine alteration phases in shergottite ALHA 77005; Information from 4.2
525 degrees K Mössbauer spectra. NASA Technical Memo 4130, 211-212.
526 Burns, R.G. (1993) Mineralogical Applications of Crystal Field Theory, 2nd ed. Cambridge, 551
527 pp.
528 Burns R.G., Parkin K.M., Loeffler B.M., Leung I.S., and Abu-Eld R.M. (1976) Further
529 characterization of spectral features attributed to titanium on the Moon. Proceedings of
530 the Lunar Science Conference 7th, 2561-2578.
531 Burns, R.G., and Huggins, F.E. (1973) Visible-region absorption spectra of a $Ti^{3+}$ fassaite from
532 the Allende meteorite: A discussion. American Mineralogist, 58, 955-961.
533 Canil D., O'Neill H.St.C., Pearson D.G., Rudnick R.L., McDonough W.F., and Carswell D.A.
534 (1994) Ferric iron in peridotites and mantle oxidation states. Earth and Planetary Science
535 Letters 123, 205-220.
536 Christie D.M., Carmichael I.S.E., and Langmuir C.H. (1986) Oxidation states of mid-ocean ridge
537 basalt glasses. Earth and Planetary Science Letters 79, 397–411.
538 Cloutis E.A. (2002) Pyroxene reflectance spectra: Minor absorption bands and effects of
539 elemental substitutions. Journal of Geophysical Research 107, doi:
540 10.1029/2001JE001590.
541 Cosca, M.A., and Peacor, D.R. (1987) Chemistry and structure of esseneite ($CaFe^{3+}AlSiO_6$), a
542 new pyroxene produced by pyrometamorphism. American Mineralogist 72, 148-156.

Cottrell E., Kelley K.A., Lanzirotti A., and Fischer R.A. (2009) High-precision determination of iron oxidation state in silicate glasses using XAS. Chemical Geology 268, 167-179.
Dowty, E., and Lindsley, D.H. (1973) Mössbauer spectra of synthetic hedenbergite-ferrosilite pyroxenes. American Mineralogist, 58, 850-868.
Dyar M.D., Klima, R.L., Fleagle, A., and Peel, S.E. (2013) Fundamental Mössbauer parameters of synthetic Ca-Mg-Fe pyroxenes. American Mineralogist, 98, 1172-1186.
Dyar M.D., Mackwell S.M., McGuire A.V., Cross L.R., and Robertson J.D. (1993) Crystal chemistry of $Fe^{3+}$ and $H^{+}$ in mantle kaersutites: Implications for mantle metasomatism. American Mineralogist, 78, 968-979.
Dyar M.D., McGuire A.V., and Mackwell S.M. (1992) $Fe^{3+}/H^{+}$ and D/H in mantle kaersutites - Misleading indicators of mantle source fugacities. Geology 20, 565-568.
Dyar M.D., McGuire A.V., and Ziegler R.D. (1989) Redox equilibria and crystal chemistry of coexisting minerals from spinel lherzolite mantle xenoliths. American Mineralogist 74, 969-980.
Dyar, M.D., Klima, R.L., and Pieters, C.M. (2007) Effects of differential recoil-free fraction on ordering and site occupancies in Mössbauer spectroscopy of orthopyroxenes. American Mineralogist, 92, 424–428.
Dyar, M.D., McGuire, A.V., and Harrell, M.D. (1992) Crystal chemistry of iron in two styles of metasomatism in the upper mantle. Geochimica et Cosmochimica Acta, 56, 2579-2586.
Ghose, S., Okamura, F.P., and Ohashi, H. (1986) The crystal structure of $CaFe^{3+}SiAlO_6$ and the crystal chemistry of $Fe^{3+}$-$Al^{3+}$ substitution in calcium Tschermak's pyroxene. Contributions to Mineralogy and Petrology, 92, 530-535.
Ghose, S., Wan, C., Okamura, F.P., Ohashi, H., and Weidner, J.R. (1975) Site preference and crystal chemistry of transition metal ions in pyroxenes and olivines. Acta Crystallographica, sect. A , 31, 76.
Hamilton V.E. (2000) Thermal infrared emission spectroscopy of the pyroxene mineral series. Journal of Geophysical Research 105, 9701-9716.
Hazen R. M., Bell P. M., and Mao H. K. 1978. Effects of compositional variation on absorption spectra of lunar pyroxenes. Proceedings, 9th Lunar and Planetary Science Conference. pp. 2919–2934.
Hinrichs J.L., Lucey P.G., Robinson M.S., Meiborn A., and Krot A.N. (1999) Implications of temperature-dependent near-IR spectral properties of common minerals and meteorites for remote sensing of asteroids. Geophysical Research Letters 26, 1661-1664.
Hörz F. (1970) A small ballistic range for impact metamorphism studies. NASA Technical Note D-5787. Washington, D.C.: National Aeronautics and Space Administration. 19 p.
Jeanloz R. and Ahrens T.J. (1977) Pyroxenes and olivines: Structural implications of shock-wave data for high pressure phases. In: High-Pressure Research (eds. M.H. Manghnani and S-I. Akimoto), p.439-461.
Johnson J.R., Hörz F., Lucey P.G., and Christensen P.R. (2002) Thermal infrared spectroscopy of experimentally shocked anorthosite and pyroxenite: Implications for remote sensing of Mars. Journal of Geophysical Research 107, doi:10.1029/2001JE001517.
Klima R.L., Dyar M.D., and Pieters C.M. (2011) Near-infrared spectra of clinopyroxenes: Effects of calcium content and crystal structure. Meteoritics & Planetary Science 46, 379-395.

587 Klima R.L., Pieters C.M., and Dyar M.D. (2007) Spectroscopy of synthetic Mg-Fe pyroxenes I:
588 Spin-allowed and spin-forbidden crystal field bands in the visible and near-infrared.
589 Meteoritics and Planetary Science 42, 235-253.
590 Klima, R. L., Pieters, C. M., and Dyar, M.D. (2008) Characterization of the 1.2 μm M1 pyroxene
591 band: Extracting cooling history from near-IR spectra of pyroxenes and pyroxene-
592 dominated rocks. *Meteoritics and Planetary Science*, 43, 1591-1604.
593 Klima, R.L., Dyar, M. D., and Pieters, C. M. (2010) Near-infrared spectra of clinopyroxenes:
594 effects of calcium content and crystal structure. *Meteoritics and Planetary Science*, doi:
595 10.1111/j.1945-5100.2010.01158.x.
596 Kress V. and Carmichael I.S.E. (1991) The compressibility of silicate liquids containing Fe2O3
597 and the effect of composition, temperature, oxygen fugacity, and pressure on their redox
598 states. Contributions to Mineralogy and Petrology 108, 82–92.
599 Kurepin, V.A., Polshin, 8.V., and Alibekov, G.I. (1981) Intracrystalline distribution of the
600 cations $Fe^{3+}$ and Al in the clinopyroxene $CaFe^{3+}AlSiO_6$. Mineralogisheskii Zhurhal, 3,
601 83-88.
602 Lindsley D.H. and Anderson D.J. (1983) A two-pyroxene thermometer. Journal of Geophysical
603 Research 88, A887-A906.
604 Mao, H.-K. (1970) The system jadeite ($NaAlSi_2O_6$)-anorthite ($CaAl_2Si_2O_8$) at high pressure.
605 Carnegie Institution of Washington Yearbook 69, 163-168.
606 Mao, H.-K.,and Bell, P.M. (1971) Crystal field spectra. Annual Report of the Geophysical
607 Laboratory Yearbook, 70, 207-215.
608 Mattioli G.S., and Wood B.J. (1988) Magnetite activities across the MgAl2O4-Fe3O4 spinel
609 join, with application to thermobarometric estimates of upper mantle oxygen fugacity.
610 Contributions to Mineralogy and Petrology 98, 148-162.
611 McCanta M.C. and Dyar M.D. (2017) Impact-related thermal effects on the redox state of Ca-
612 pyroxene. Meteoritics and Planetary Science, doi: 10.1111/maps.12793.
613 McGuire A.V., Dyar M.D., and Nielson J.E. (1991) Metasomatic oxidation of upper mantle
614 peridotite. Contributions to Mineralogy and Petrology 109, 252-264,
615 doi:10.1007/BF00306483.
616 McGuire, A.V., Dyar, M.D., and Ward, K.W. (1989) Neglected $Fe^{3+}/Fe_{2+}$ ratios: a study of $Fe^{3+}$
617 contents of megacrysts from alkali basalts. *Geology*, 17, 687-689.
618 Mustard J.F., Poulet F., Gendrin A., Bibring J.P., Langevin Y., Gondet B., Mangold N., Bellucci
619 G., and Altieri F. (2005) Olivine and pyroxene, diversity in the crust of Mars. Science
620 307:1594-1597.
621 Ohashi, H., and Hariya, Y. (1970) Order-disorder of ferric iron and aluminum in Ca-rich
622 clinopyroxene. Proceedings of the Japanese Academy, 46, 684-687.
623 Ostertag R., Amthauer G., Rager H., and McSween H.Y. Jr. (1984) $Fe^{3+}$ in shocked olivine
624 crystals of the ALHA 77005 meteorite. Earth and Planetary Science Letters 67, 162-166,
625 doi:10.1016/0012-821X(84)90111-0.
626 Papike J.J., Simon S.B., Burger P.V., Bell A.S., Shearer C.K., and Karner J.M. (2016)
627 Chromium, vanadium, and titanium valence systematics in Solar System pyroxene as a
628 recorder of oxygen fugacity, planetary provenance, and processes. American
629 Mineralogist 101, 907-918.
630 Pelkey S.M., Mustard J.F., Murchie S., Clancy R.T., Wolff M., Smith M., Milliken R., Bibring
631 J.-P., Gendrin A., Poulet F., Langevin Y., and Gondet B. (2007) CRISM multispectral

summary products: Parameterizing mineral diversity on Mars from reflectance. Journal of Geophysical Research Planets, 112, doi.org/10.1029/2006JE002831.
Peslier A.H., Hervig R., Yang S., Humayun M., Barnes J. J., and Brandon A.D. (2019) Determination of the water content and D/H ratio of the martian mantle by unraveling degassing and crystallization effects in nakhlites. Geochimica et Cosmochimica Acta 266, 382–415.
Pieters C.M. (1993) Compositional diversity and stratigraphy of the lunar crust derived from reflectance spectroscopy. In Remote geochemical analysis: Elemental and mineralogical composition (eds. Pieters C.M. and Englert P.A.J.). Cambridge University Press. pp. 309-339.
Pieters C.M. and Hiroi T. (2004) RELab (Reflectance Experiment Laboratory): A NASA multiuser spectroscopy facility. 35th Lunar and Planetary Science Conference, abstract #1720.
Pieters C.M., Klima R.L., Hiroi T., Dyar M.D., Lane M.D., Treiman A.H., Noble S.K., Sunshine J.M., and Bishop J.L. (2008) Martian dunite NWA 2737: Integrated spectroscopic analyses of brown olivine. Journal of Geophysical Research 113, doi:10.1029/2007JE002939.
Rossi, G., Oberti, R., Dal Negro, A., Molin, G.M., and Mellini, M. (1987) Residual electron density of the M2 site in C2/c clinopyroxenes relationship with bulk chemistry and sub-solidus evolution. Physics and Chemistry of Minerals, 14, 514–520.
Rossman, G.R. (1980) Pyroxene spectroscopy. Reviews in Mineralogy, 7, 91-115,
Sack R.O., Carmichael I.S.E., Rivers M.L., and Ghiorso M.S. (1980) Ferric-ferrous equilibria in natural silicate liquids at 1 bar. Contributions to Mineralogy and Petrology 75, 369–376.
Seifert, F. (1983) Mössbauer line broadening in aluminous orthopyroxenes: Evidence for next nearest neighbors interactions and short-range order. NeuesJ ahrbuch fiir Mineralogie Abhandlungen, 148, 14l-162.
Shankland, T.J., Duba, A. G., and Woronow, A. (1974) Pressure shifts of optical absorption bands in iron-bearing garnet, spinel, olivine, pyroxene, and periclase. Journal of Geophysical Research, 79, 3273-3282.
Straub D.W., Burns R.G., and Pratt S.F. (1991) Spectral signatures of oxidized pyroxenes: Implications to remote sensing of terrestrial planets. Journal of Geophysical Research 96, 18,819–18,830.
Straub, D.W. and Burns, R.G. (1991) Degradation of Fe-Mg silicates in hot CO2 atmospheres: Applications to Venus. LPSC, XXII, 1349-1350.
Straub, D.W., Burns, R.G., and Pratt, S.F. (1991) Spectral signature of oxidized pyroxenes: implications to remote-sensing of terrestrial planets. Journal of Geophysical Research, 96, 18819-18830.
Sung, C.-M., Singer, R.B., Parkin, K.M., and Burns, R.G. (1977) Temperature dependence of $Fe^{2+}$ crystal field spectra: Implications to mineralogical mapping of planetary surfaces. Proceedings Lunar Science Conference 8th, 1063-1079.
Treiman A.H., Dyar M.D., McCanta M.C., Pieters C.M., Hiroi T., Lane M.D., and Bishop J. (2007) Martian dunite NWA 2737: Petrographic constraints on geologic history, shock events, and olivine color. Journal of Geophysical Research 112, doi:10.1029/2006JE002777.
Turnock A.C., Lindsley D.H., and Grover J.E. (1973) Synthesis and unit cell parameters of Ca-Mg-Fe pyroxenes. American Mineralogist 58, 50-59.

678 White, W.B., and Keester, K.L. (1966) Optical absorption spectra of iron in the rock-forming
679 silicates. American Mineralogist, 51, 774-791.
680 Wood B.J. (1991) Oxygen barometry of spinel peridotites. Reviews in Mineralogy 25, 417-431.
681 Zhang L., Ahsbahs H., Hafner S.S., and Kutoglu A. (1997) Single-crystal compression and
682 crystal structure of clinopyroxene up to 10 GPa. American Mineralogist 82, 245 - 258.
683 Zhi, X.C., Chen, P., Lin, C.Z., Chen, S.Q., Zhang,m G.L.n Li, Y.Z., and Lin, L. (2001) Oxidation
684 experiment of natural megacrystal clinopyroxene: Implications for assignment of Mossbauer
685 spectra. Acta Geologica Sinicia – English edition, 75, 51-58.
686

Table 1. Summary of Pyroxene Compositions.

| Sample | Locality | Wo | En | Fs | Mg# | $Fe^{3+}/\Sigma Fe$ |
|---|---|---|---|---|---|---|
| Ba-1-61 cpx | Dish Hill, CA | 46.7 | 48.2 | 5.1 | 91.9 | 16 |
| DH-210 cpx | Dish Hill, CA | 40.4 | 50.3 | 9.3 | 87.2 | 21 |
| Ba-2-101-E cpx | Dish Hill, CA | 45.8 | 49.0 | 5.1 | 93.3 | 32 |
| DH-218 cpx | Dish Hill, CA | 43.6 | 42.7 | 13.7 | 82.3 | 34 |
| DH-201 cpx | Dish Hill, CA | 43.8 | 44.3 | 11.9 | 85.1 | 35 |
| DH-211 cpx | Dish Hill, CA | 43.3 | 43.5 | 13.3 | 83.2 | 35 |
| DH-213 cpx | Dish Hill, CA | 44.0 | 43.3 | 12.6 | 84.0 | 36 |
| DH-231 cpx | Dish Hill, CA | 43.8 | 41.9 | 14.3 | 81.9 | 37 |
| DH-217 cpx | Dish Hill, CA | 44.3 | 42.0 | 13.7 | 82.9 | 39 |
| DH-101-E opx | Dish Hill, CA | 1.6 | 89.8 | 8.6 | 91.7 | 6 |
| Ba-2-101-B opx | Dish Hill, CA | 1.2 | 80.8 | 8.5 | 90.5 | 9 |
| Ba-2-101-D opx | Dish Hill, CA | 9.3 | 82.6 | 8.1 | 92.2 | 14 |
| EP-3-72 cpx | Kilbourne Hole, NM | 46.2 | 48.5 | 5.3 | 91.9 | 18 |
| EP-3-162 cpx | Kilbourne Hole, NM | 46.6 | 47.4 | 5.9 | 91.1 | 22 |
| EP-1-42A cpx | Kilbourne Hole, NM | 51.5 | 46.7 | 0.7 | 74.9 | 25 |
| EP-1-42B cpx | Kilbourne Hole, NM | 46.2 | 41.0 | 0.70 | 69.5 | 25 |
| EP-3-72 opx | Kilbourne Hole, NM | 1.7 | 88.6 | 9.7 | 90.8 | 4 |
| Ki-5-235 cpx | Cima, CA | 46.5 | 48.3 | 5.2 | 91.7 | 16 |
| Jaipur diopside[a] | Jaipur, India | 49.3 | 47.0 | 3.7 | 94.8 | 8 |
| 3493 (36 GPa)[b] | Jaipur, India | 49.3 | 47.0 | 3.7 | 94.8 | 31 |
| 3494 (43 GPa) | Jaipur, India | 49.3 | 47.0 | 3.7 | 94.8 | 24 |
| 3496 (52 GPa) | Jaipur, India | 49.3 | 47.0 | 3.7 | 94.8 | 17 |
| 3495 (59 GPa) | Jaipur, India | 49.3 | 47.0 | 3.7 | 94.8 | 27 |

[a]Composition from McCanta and Dyar [2017]

[b]Shock sample pressure in parentheses from McCanta and Dyar [2017]

687

688

## Figure Captions

Figure 1. Portions of the crystal structures of the $Fe^{3+}$ (left) and $Fe^{2+}$ (center and right) forms of Ca clinopyroxene, essenite from Cosca and Peacor [1987] and hedenbergite from Zhang et al. [1997], at 0 GPa (center) and 10 GPa (right). In these nominal end-members, Ca fills the M2 site and Fe the M1 site, but in most naturally occurring pyroxenes, Mg, $Fe^{2+}$, and $Fe^{3+}$ compete for the M1 site, and some $Fe^{2+}$ also enters the M2 site.

Figure 2. Comparison of bond distances for the three pyroxenes for which structures are shown in Figure 1. Esseneite is the $Fe^{3+}$ clinopyroxene that forms in fused sedimentary rocks. The two hedenbergite refinements are taken from Zhang et al. [1987] from the same sample at ambient and 10 GPa. The $Fe^{3+}$ sample behaves more like the high-pressure hedenbergite and supports the idea that both high pressure and small cations affect bond distances.

Figure 3. Pyroxene quadrilateral showing the range of pyroxene compositions investigated in this study in red squares.

Figure 4. Visible and near-infrared spectra of mantle clinopyroxene. Spectra are offset for clarity. Spectral line color indicates amount of $Fe^{3+}$ measured in the pyroxene (%$Fe^{3+}$ values for individual pyroxenes listed in Table 1). Red = 35-39%$Fe^{3+}$; orange = 30-34%$Fe^{3+}$; green = 20-29%$Fe^{3+}$; blue = 10-19%$Fe^{3+}$; purple = 8%$Fe^{3+}$. Location of the $Fe^{2+}\leftrightarrow Fe^{3+}$ IVCT band is shown as the black dashed line. Note the shift to lower wavelengths as a function of progressive oxidation. Location of the spin-forbidden crystal $Fe^{3+}$ feature at 0.44 μm is shown as black dash-dot line.

Figure 5. Visible and near-infrared spectra of mantle orthopyroxenes. Spectra are offset for clarity. Numbers on right side of plot indicate the %$Fe^{3+}$ measured in each pyroxene. Location of the $Fe^{2+}\leftrightarrow Fe^{3+}$ IVCT band is shown as the black dashed line.

Figure 6. Visible and near-infrared spectra of shocked clinopyroxenes and unshocked starting material. Spectra are offset for clarity. Numbers on right side of plot indicate the %$Fe^{3+}$ measured in each pyroxene. Experimental shock pressures are given on the left side of the plot.

Figure 7. Relationship between spectral slope between 0.4 and 0.6 μm (absorption edge) and %$Fe^{3+}$. Slope calculated using the median of 3 channels on either side of respective wavelength to reduce stochastic noise. Green triangles = shocked clinopyroxene; green star = shocked clinopyroxene starting composition; red squares = mantle clinopyroxene; blue circles = mantle orthopyroxene.

Figure 8. Mid-infrared spectra of shocked clinopyroxenes and unshocked starting material. Spectra are offset for clarity. Numbers on right side of plot indicate the %$Fe^{3+}$ measured in each pyroxene. Experimental shock pressures are given on the left side of the plot. Dashed lines indicate the critical absorptions (CA1-CA5) identified by Hamilton [2000] for high Mg clinopyroxene and the additional 515 $cm^{-1}$ absorption observed in high Mg pyroxenes.

Figure 9. Mid-infrared spectra of selected mantle clinopyroxene. Spectra are offset for clarity. Numbers on left side of plot indicate the $\%Fe^{3+}$ measured in each pyroxene. Dashed lines indicate the critical absorptions (CA1, CA2+CA3, CA4, CA5) identified by Hamilton [2000] for high Mg clinopyroxene and the additional 515 $cm^{-1}$ absorption observed in high Mg pyroxenes.

Figure 10. Mid-infrared spectra of mantle orthopyroxene. Spectra are offset for clarity. Numbers on left side of plot indicate the $\%Fe^{3+}$ measured in each pyroxene. Dashed lines indicate the critical absorptions (CA1-CA8) identified by Hamilton [2000] for high Mg orthopyroxene.

Figure 11. Comparison of VNIR spectra of mantle oxidized clinopyroxene ($\%Fe^{3+} = 35$) and shocked clinopyroxene ($\%Fe^{3+} = 31$).

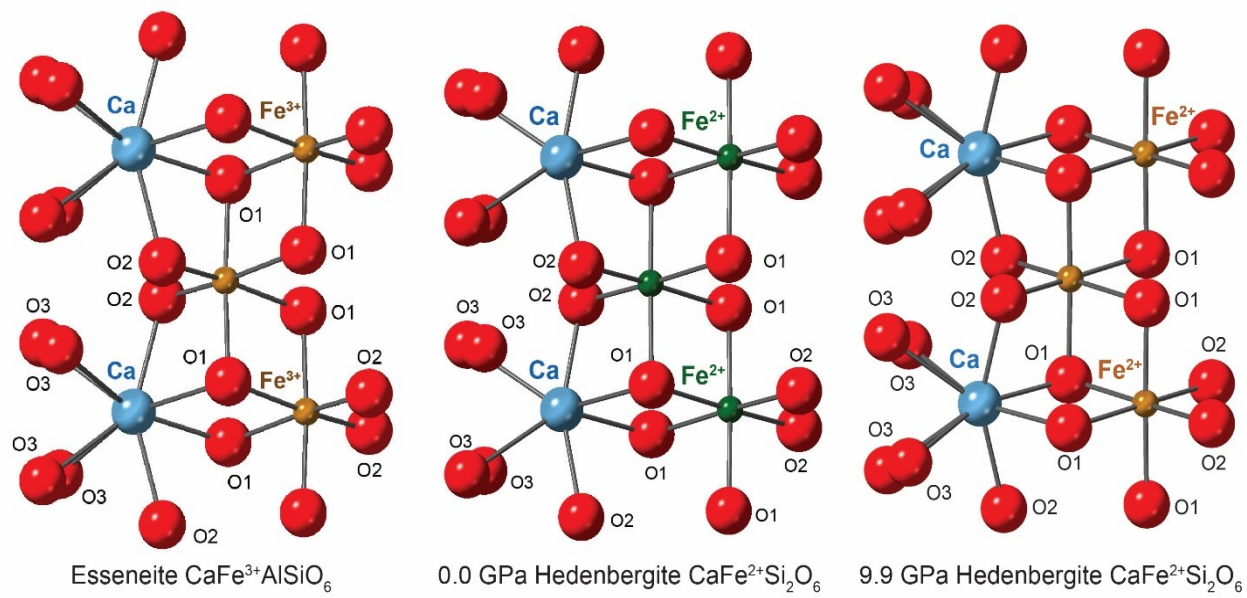


747
748 Figure 1.
749

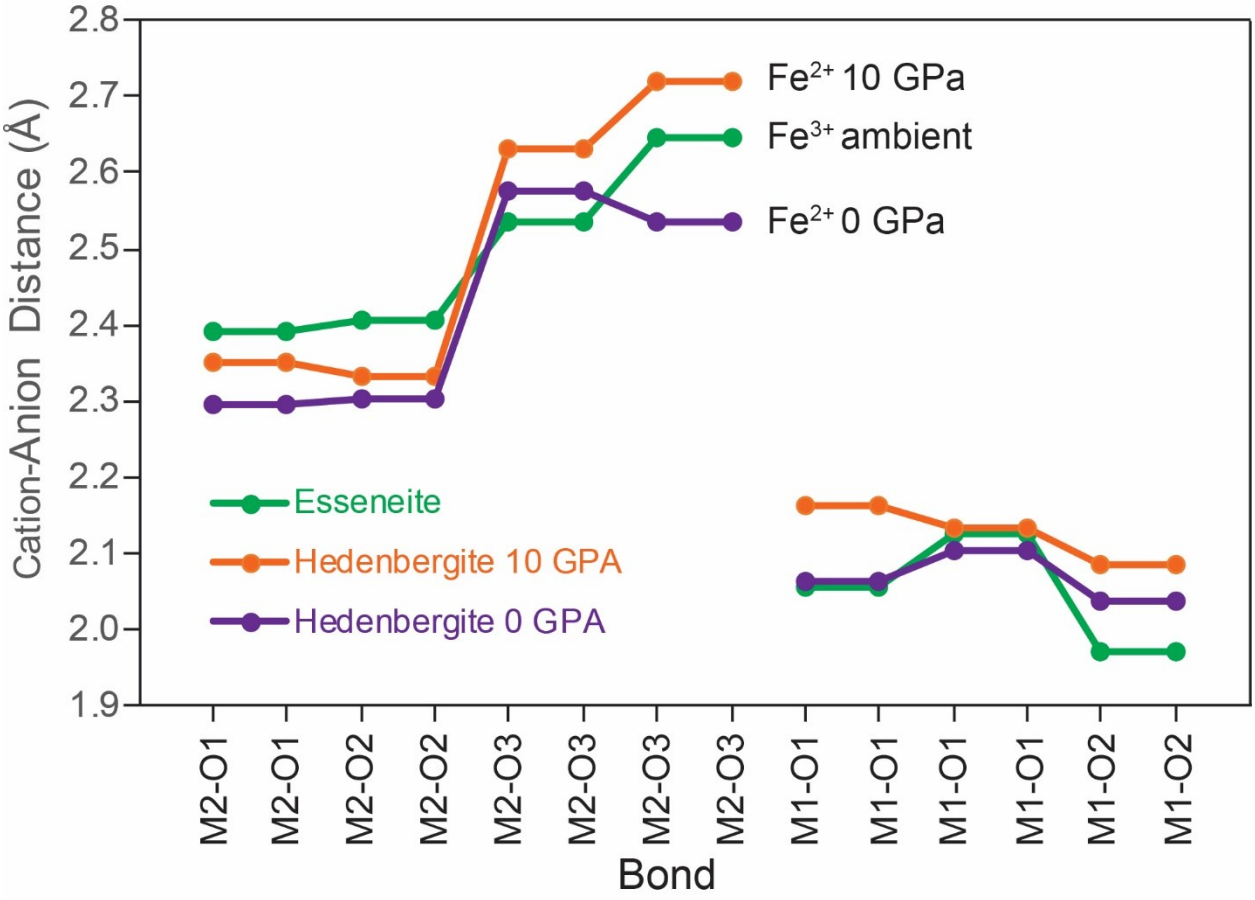
Cation-Anion Distance (Å)
2.8
2.7
2.6
2.5
2.4
2.3
2.2
2.1
2.0
1.9
Fe2+ 10 GPa
Fe3+ ambient
Fe2+ 0 GPa
Esseneite
Hedenbergite 10 GPA
Hedenbergite 0 GPA
M2-O1
M2-O1
M2-O2
M2-O2
M2-O3
M2-O3
M2-O3
M2-O3
M1-O1
M1-O1
M1-O1
M1-O1
M1-O2
M1-O2
Bond

Figure 2.

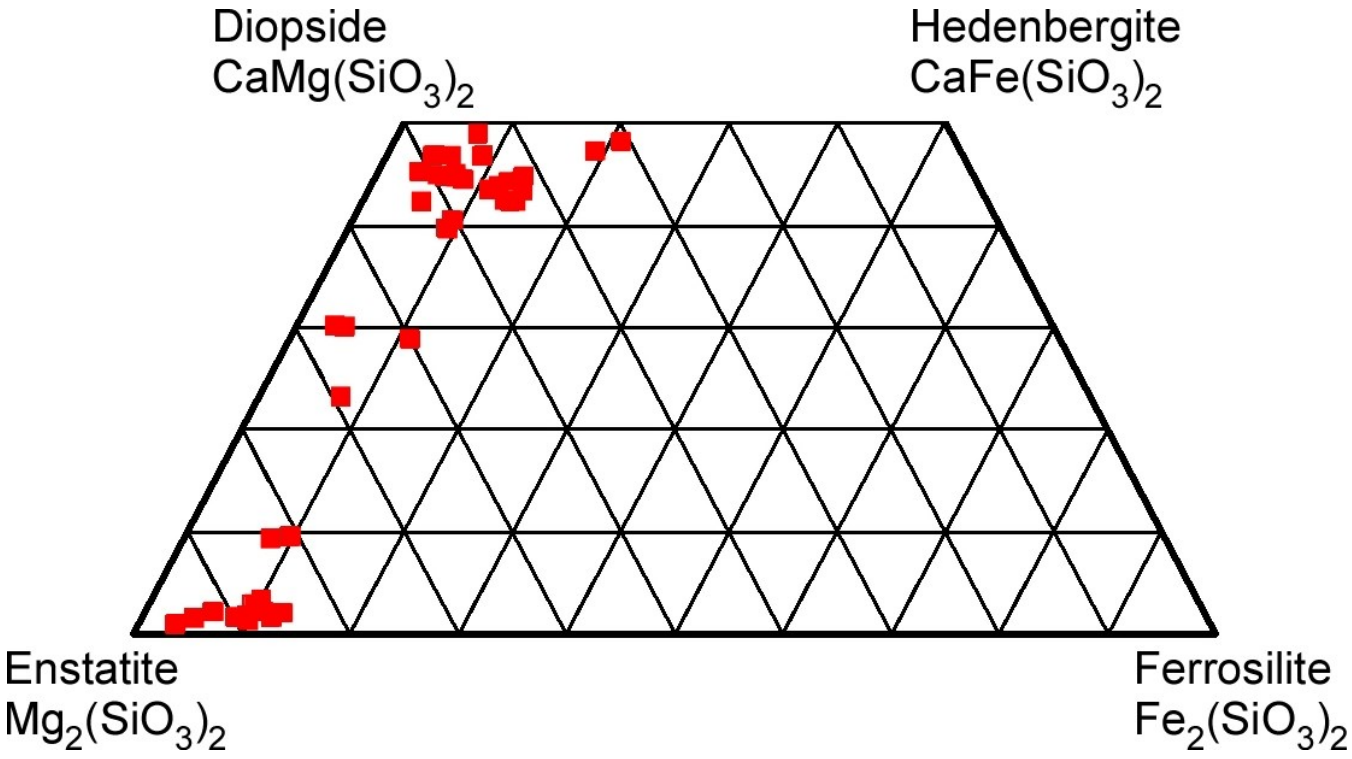


754
755 Figure 3.
756
757

758

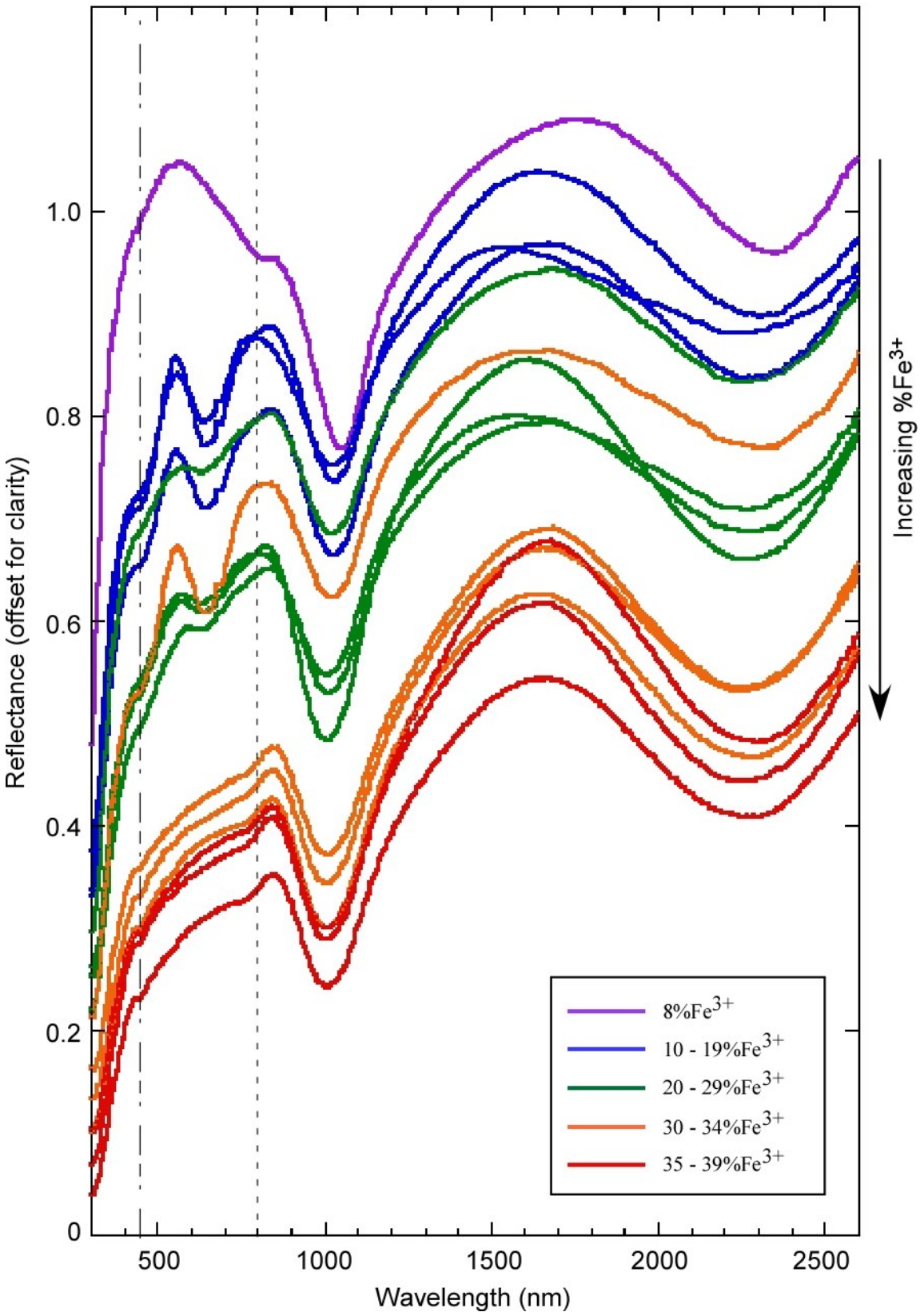
Reflectance (offset for clarity)
Wavelength (nm)
0
0.2
0.4
0.6
0.8
1.0
500
1000
1500
2000
2500
Increasing %Fe3+
8%Fe3+
10 - 19%Fe3+
20 - 29%Fe3+
30 - 34%Fe3+
35 - 39%Fe3+

Figure 4

759

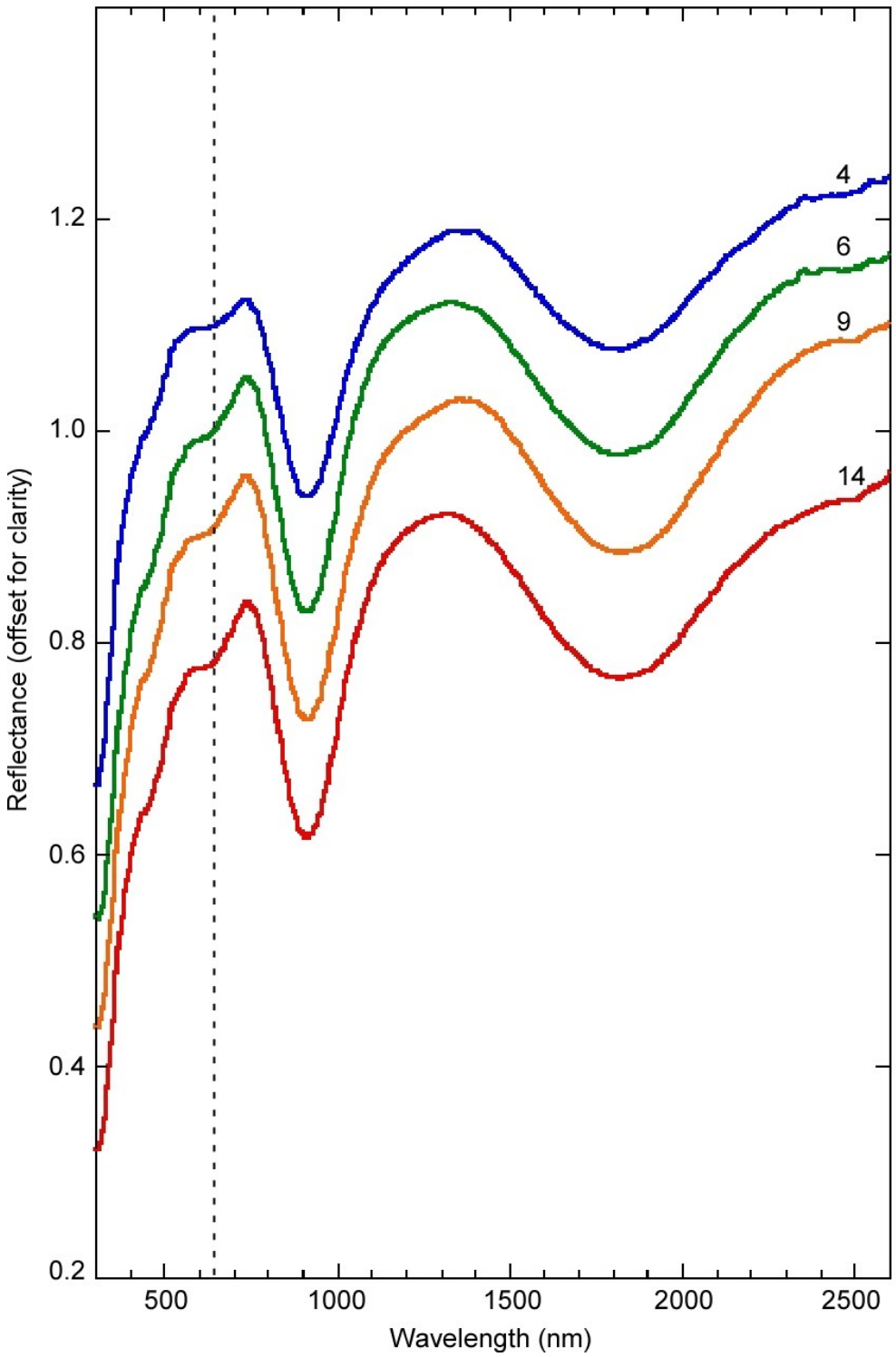


760 Figure 5.

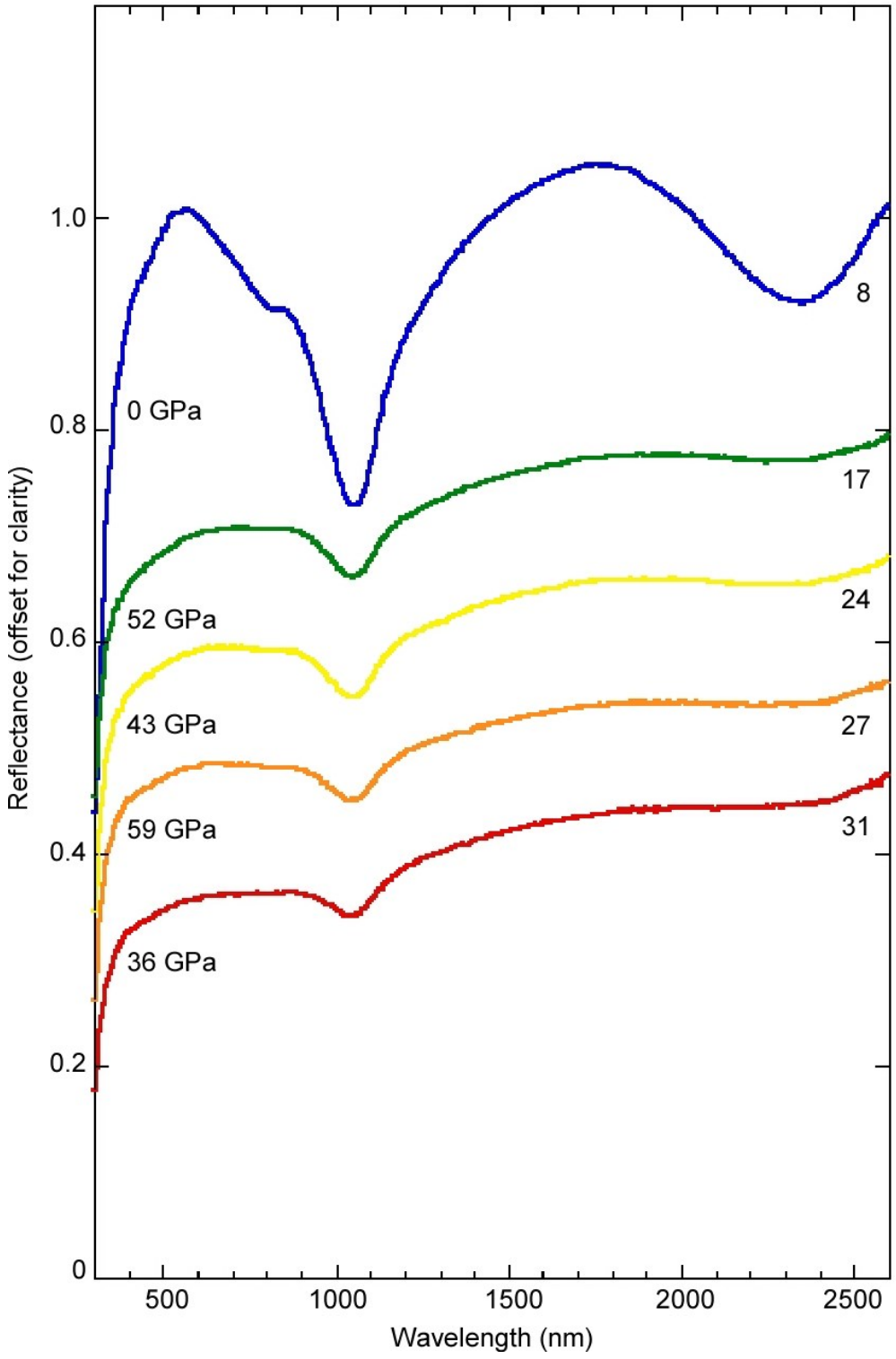


761 Figure 6.
762

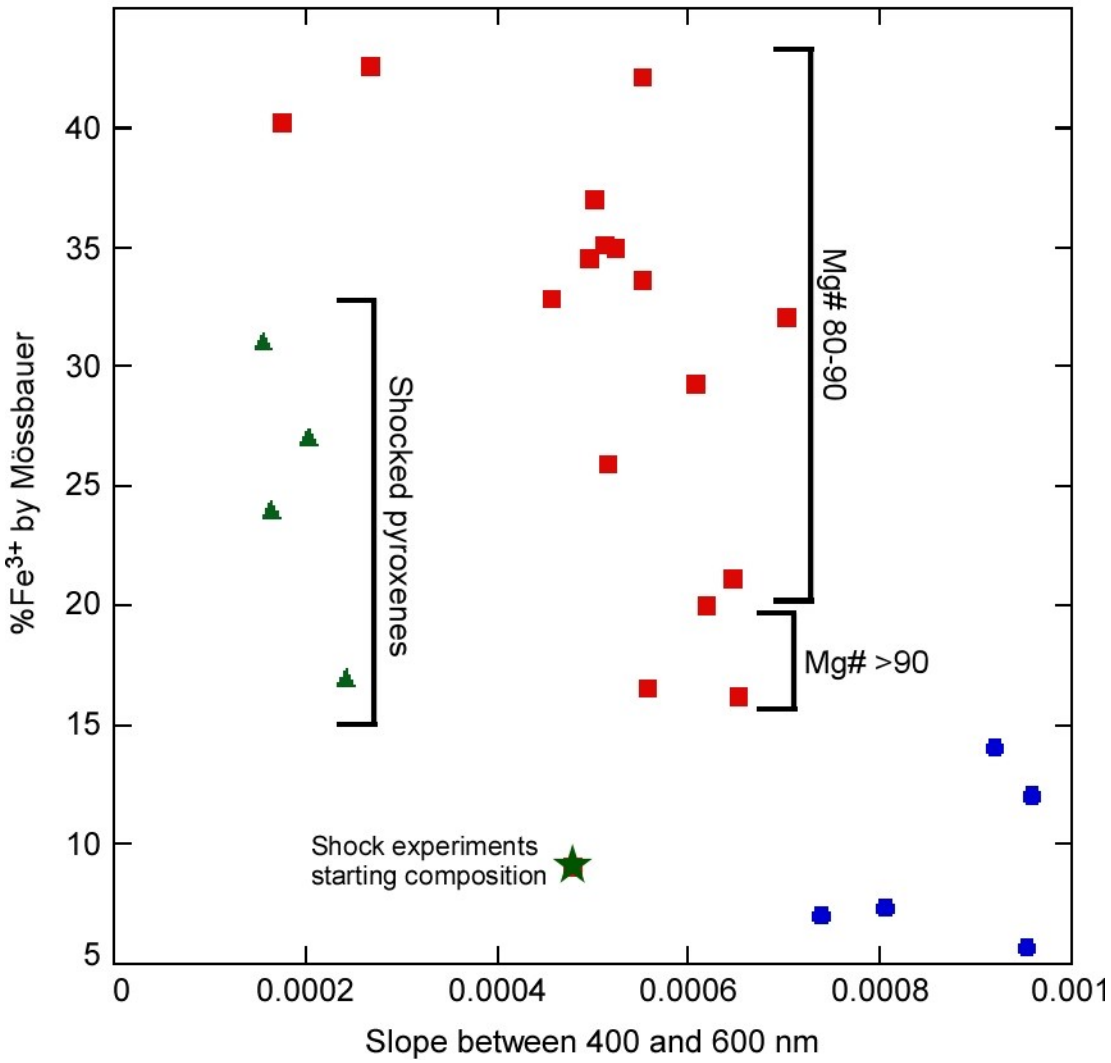


Figure 7.

763
764

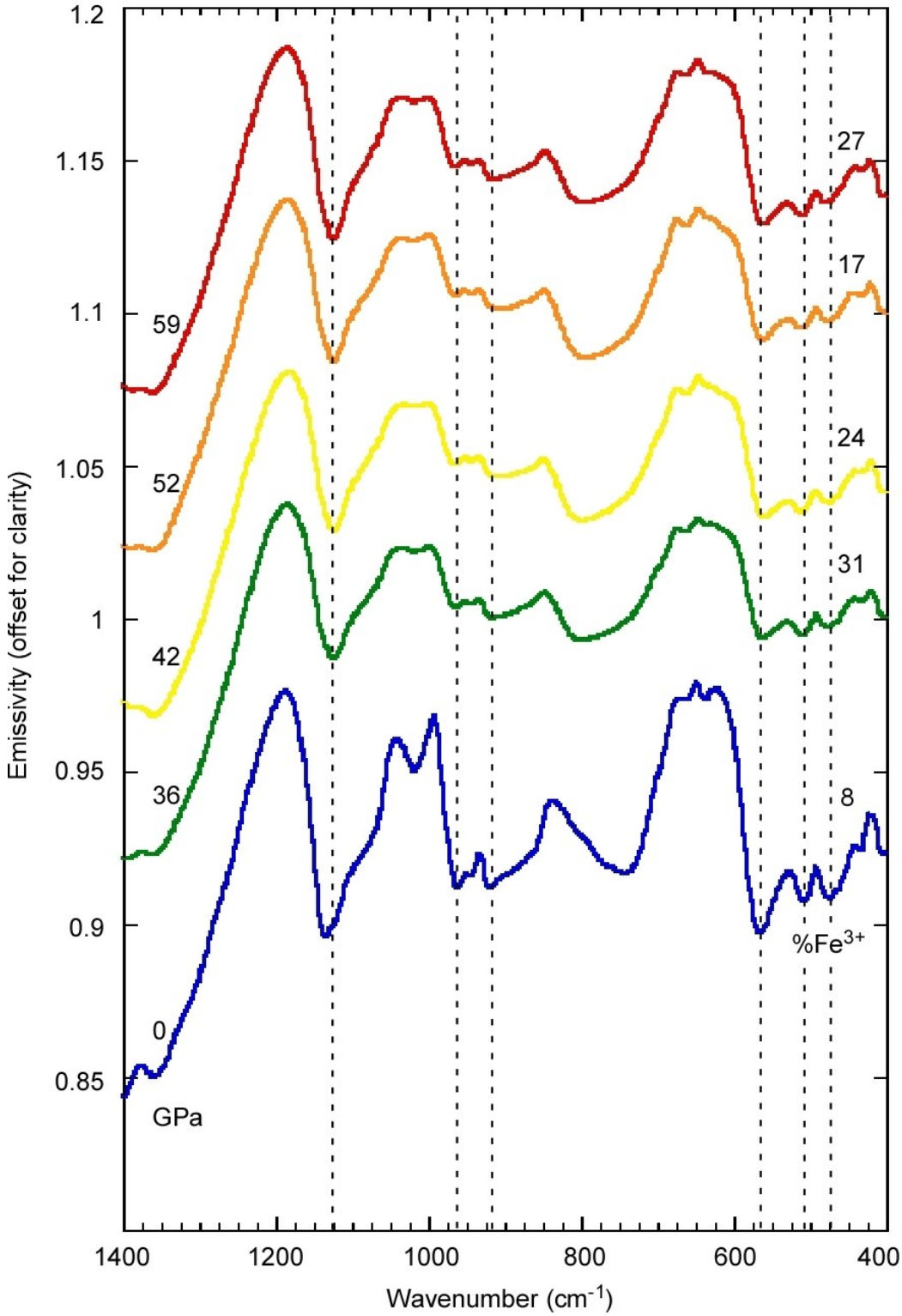


765 Figure 8.
766

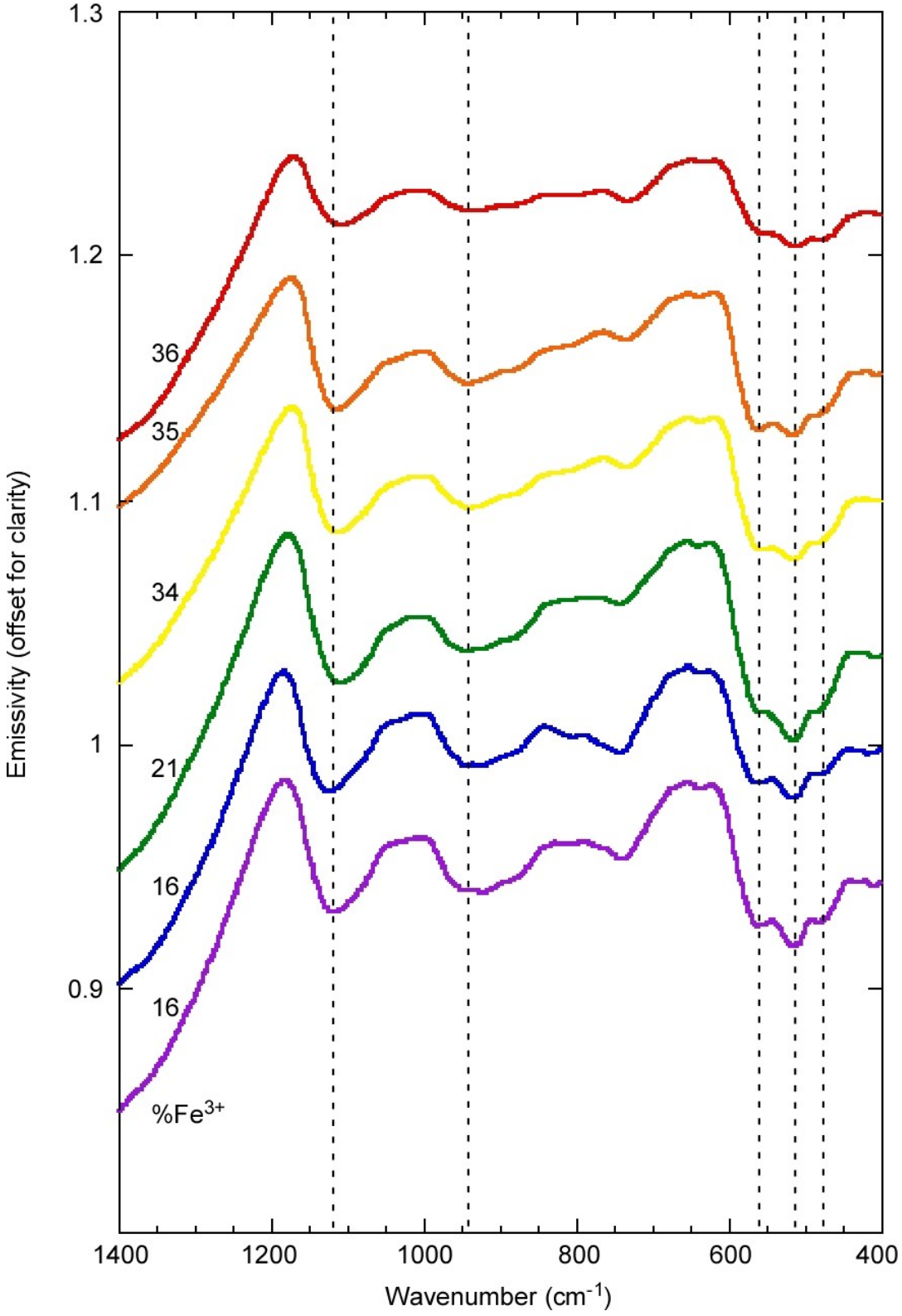
1.3
1.2
1.1
1
0.9
Emissivity (offset for clarity)
36
35
34
21
16
16
%Fe3+
1400
1200
1000
800
600
400
Wavenumber (cm-1)

Figure 9.

767

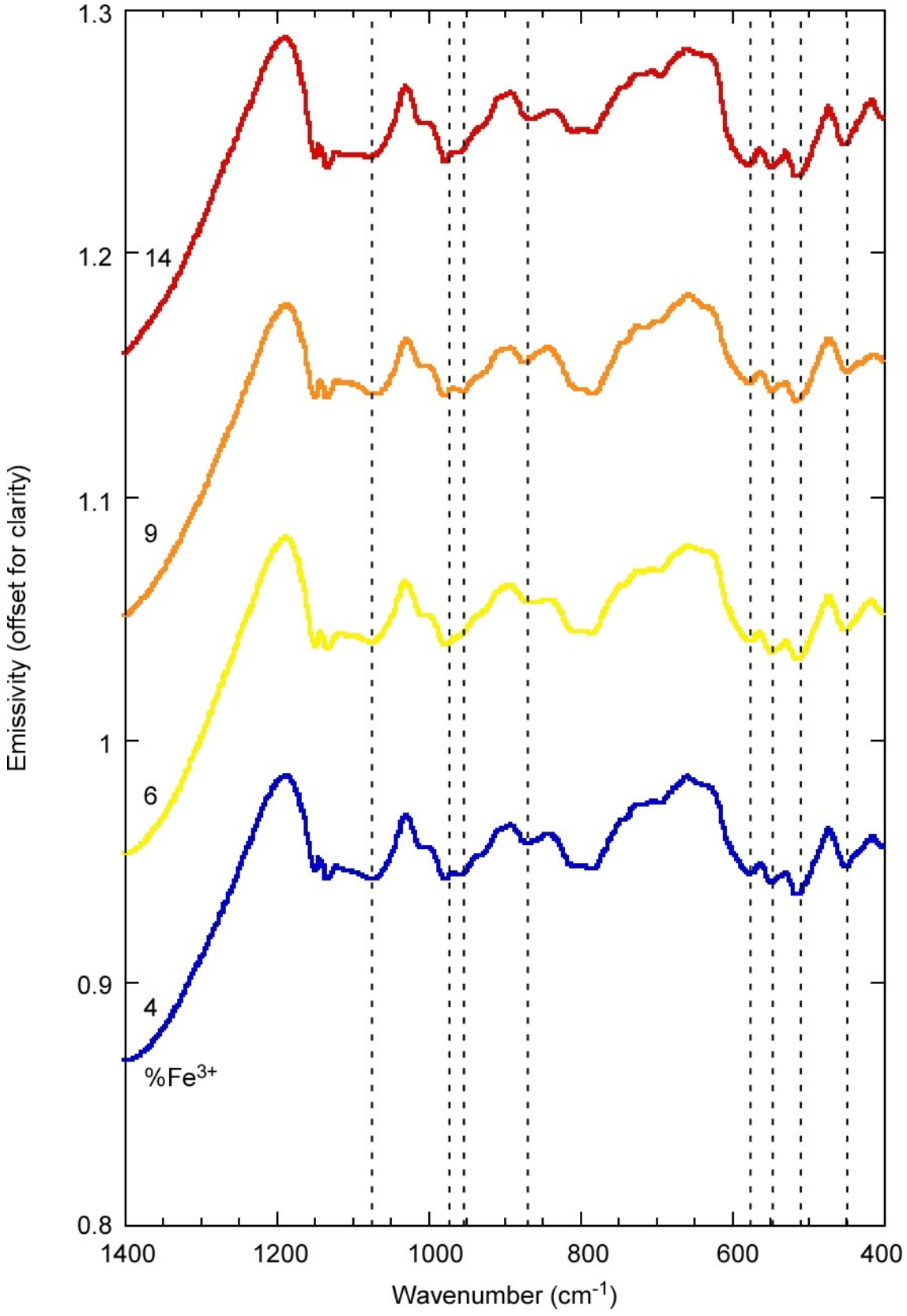


768 Figure 10.

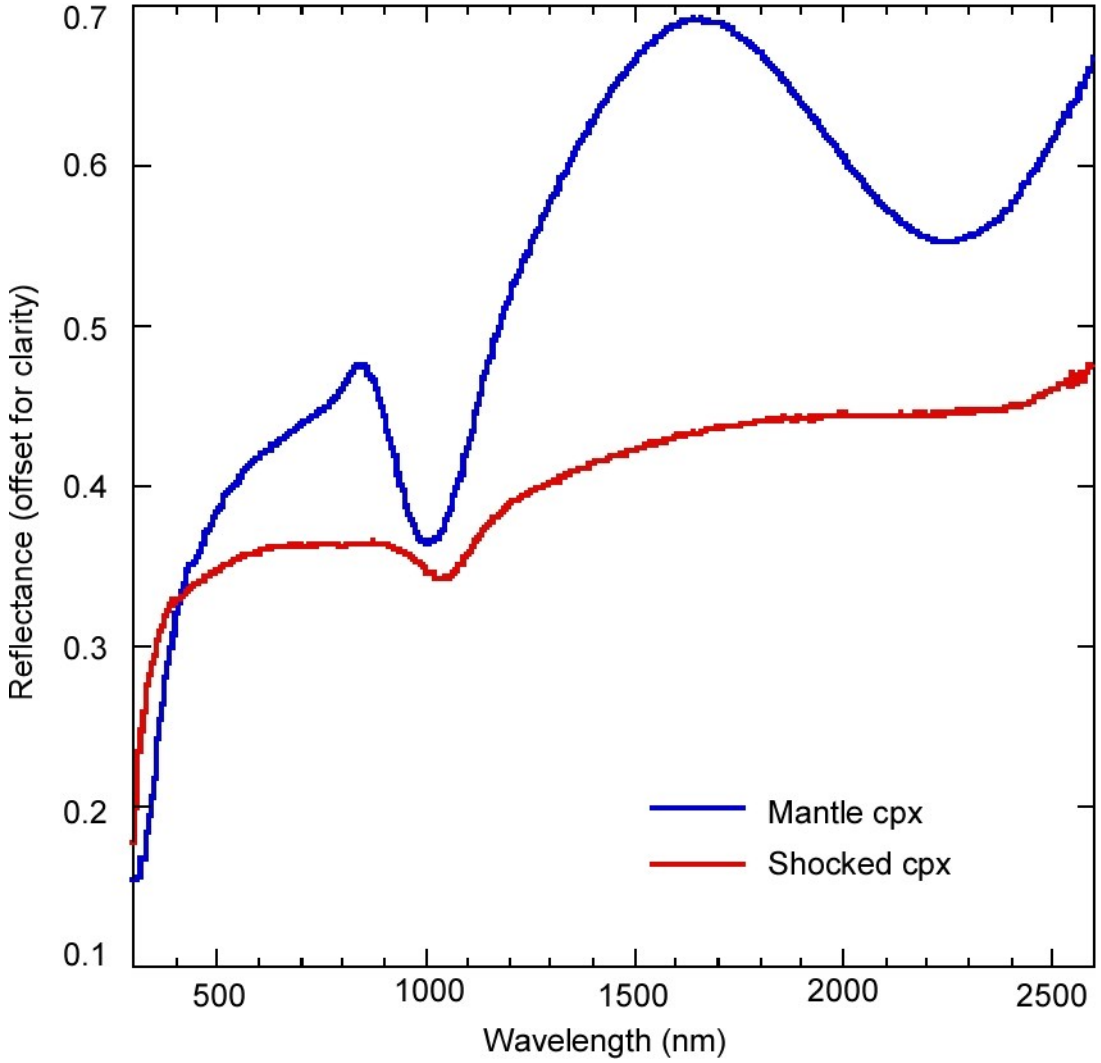


769

770 Figure 11.